

Study of extensive air showers and primary energy spectra by MAKET-ANI detector on mountain Aragats

A. Chilingarian^a, G. Gharagozyan^a, S. Ghazaryan^a, G. Hovsepyan^{a,b,*},
E. Mamidjanyan^{a,b}, L. Melkumyan^a, V. Romakhin^{b,✱}, A. Vardanyan^a, S. Sokhoyan^{a,b}

^a Alikhanyan Physics Institute, Cosmic Ray Division, Armenia

^b Lebedev Physics Institute, Moscow, Russia

Received 20 November 2006; received in revised form 17 April 2007; accepted 20 April 2007
Available online 27 April 2007

Abstract

Small and middle size surface detectors measuring extensive air showers (EAS) initiated by primary cosmic rays (PCR) incident on terrestrial atmosphere have been in operation for the last 50 years. Their main goal is to explore the “knee” in all particle spectrum to solve the problem of cosmic ray (CR) origin and acceleration. The recent achievements of atmospheric Cherenkov telescopes and X-ray space laboratories, establishing the supernova remnants (SNRs) as a source of hadronic cosmic rays, pose stringent conditions on the quality of EAS evidence. After establishing the existence of the “knee” itself, the most pronounced result from EAS studies is the rigidity dependent shift of the knee position to the highest energies. This feature was first observed by separation of the primary flux in different mass groups in MAKET-ANI, EAS-TOP and KASCADE experiments. The MAKET-ANI detector is placed on Mt. Aragats (Armenia) at 3200 m above the sea level (40°25′N, 44°15′E). More than 1.3×10^6 showers with size greater than 10^5 particles were registered in 1997–2004. The detector effectively collected the cores of EAS, initiated by primaries with energies of 10^{14} – 10^{17} eV. After proving that the quality of the EAS size and shape reconstruction was reasonably high, we present the lateral distribution function (LDF) for distances from 10 to 120 m from EAS core and EAS size spectra in 5 zenith angle intervals. We use CORSIKA simulations to present the energy spectra. The results from the MAKET-ANI experiment on the energy spectra of the “light”(p + He) and “heavy”(O + Si + Fe) nuclear groups are compared to the spectra obtained by balloon experiments and to other available spectra.
© 2007 Elsevier B.V. All rights reserved.

Keywords: EAS installation; Lateral distribution function (LDF); EAS size spectra; Cosmic ray energy spectra; “Light” and “heavy” components

0. Introduction

A new paradigm in astrophysics research consists of the detection of celestial objects in radio, optical, X-rays, and gamma rays. A variety of compatible measurements provide sufficient information for building realistic models of physical processes of supernovae explosions, of accompanying gamma-ray bursts, of accretion disc interactions with

super-dense objects, and, finally, of the evolution of Universe itself. In this case additional information about the particles of highest energies arriving in the Solar system will significantly enrich the information about the most violent processes in the Universe.

Cosmic ray (CR) flux incident on terrestrial atmosphere consists mostly of protons and heavier stripped nuclei accelerated at numerous galactic and extragalactic sites. One of the most exciting questions to be explored by cosmic rays research is that of identifying the accelerating sources and acceleration mechanisms. Due to the bending in galactic magnetic fields, charged particles lose information about the parent sites during their long travel and arrive on the Earth being highly isotropic. Galactic cosmic

* Corresponding author. Address: Alikhanyan Physics Institute, Cosmic Ray Division, Armenia. Tel./fax: +374 10 344 377.

E-mail address: hgg@crdlx5.yerphi.am (G. Hovsepyan).

✱ Deceased.

rays cannot map the objects where they were born, therefore, only integrated information from all sources is available from measurements of cosmic ray fluxes on the surface of Earth. This information consists of the shape of the energy spectra of the different species of cosmic rays and of the CR arrival anisotropy.

The energy spectrum is of non-thermal origin and follows a power law over many orders of magnitude. The spectrum steepens at energies around 3–5 PeV. This feature is commonly called the knee and its explanation is generally believed to be a corner stone in understanding the origin of cosmic rays [1].

Presently, cosmic rays above ~ 0.1 PeV are experimentally accessible in ground-based detectors only. These detectors do not measure the primary particles; secondary particles produced in high-energy interactions in the atmosphere and forming extensive air showers (EAS) are measured instead. This makes the interpretation of the indirect measurements very difficult and the results obtained depend on the understanding of high-energy interactions in the atmosphere. However, regardless of considerable differences of the applied methods analyzing the EAS observables, different simulation procedures, and different observation levels, the compiled experimental results agree quite well (see review [2]). After compiling the world data (14 spectra), the average values and their variances result in a slope below the knee $\gamma = -(2.68 \pm 0.06)$ and above the knee to $-(3.06 \pm 0.08)$ with the knee position at $E_k = (3.2 \pm 1.2) \times 10^{15}$ eV. Nevertheless, to understand the CR origin, the knowledge of the all-particle spectra is not enough. As [1] demonstrates, the majority of 17 different particle acceleration models yield very similar all-particle spectra. On the other hand, the predictions of the behavior of the individual element spectra are quite different.

The implementation of the non-parametric multivariate methodology [3] allows for the event-by-event-analysis of EAS data [4], using Bayesian and neural network statistical models [5–7]. These methods also allow control of the quality of statistical decisions. At each stage of the analysis, we estimate the value of the information content of the variables used for EAS classification and energy estimation and restrict the complexity of the physical inference (number of different mass groups) according to this value.

The MAKET-ANI setup is located at 3200 m above the sea level on Mt. Aragats, Armenia. At this altitude the shape of the showers is not distorted by the attenuation in the terrestrial atmosphere and it is possible to reliably reconstruct EAS size and shape. The distinctive information contained in the distributions of these two parameters allows us to classify the EAS with a high level of accuracy only into two distinct groups: initiated by “light” (p + He) or “heavy” (O + Si + Fe) nuclei. The previously published MAKET-ANI data [8] demonstrated the existence of a sharp knee in the light component, and no knee in the heavy one up to about 3×10^{16} eV. The available world data confirm these results. In the KASCADE experiment,

the position of the knee shifted towards higher energies with increasing element number [9]. In HEGRA [10] a different experimental methodic was used, nevertheless the result also shows steepening of the light mass group and a shift of the knee position to lower energy as compared to the all particle spectra. In EAS-TOP [11], the light component was separated using information from the EAS electrons and TeV muons. The results could again be interpreted in the standard framework of a rigidity-dependent acceleration/propagation process.

To summarize the situation with EAS experiments around the knee, the limiting factors of a more detailed analysis and “mass spectroscopy” in the knee region include the uncertainty of the parameters of high-energy interaction models required for the complicated “unfolding” techniques [12]. See also the discussion in [13]. More robust non-parametric statistical analysis models [14] proceeding from less sophisticated simulations and classifying EAS only into two groups allow to derive rigidity-dependent knee position [8, 15–17], as expected from the diffusive shock acceleration by Supernova (SNR) blast waves (see review [18]). We think that this is the *final physical inference* on partial energy spectra that can be drawn from small to middle size EAS experiments. This inference is supported by different experiments, statistical methods, hard interaction models and EAS parameters included in the analysis.

Another *indirect strong evidence* of the proton and ion acceleration in SNR is the strong amplification of the magnetic field. The precise measurements of the X-rays from SN 1006, by CHANDRA [19] imply a very large effective magnetic field of >100 μ G in the Supernovae remnant. In [20] the authors conclude that such a large field could be generated only by the non-linear interactions of the accelerated protons and stripped heavier nuclei with self-generated Alfvén waves in a strong shock. Therefore, the SN 1006 data confirm the acceleration of the nuclear component at least up to several units of 10^{14} eV. Further morphological measurements of young SNRs (Cas A and Tycho, Kepler, ...) prove that they all exhibit the amplification effect as a result of the very efficient acceleration of nuclear cosmic rays at the outer shock [21].

The *direct evidence* of the shock wave acceleration in SNR shells was achieved by the atmospheric Cherenkov telescopes (ACT). The measured γ -ray maps of SNR shells RX J1713.7-3946 and RX J0852.0-4622 [22] (both discovered in TeV γ -rays by CANGAROO [23]) demonstrate that the shock wave accelerates particles to multi-TeV energies, generating photons via hadron interactions with gas. This direct evidence provided by the ACT imaging technique is supported by the indirect evidences provided by the detailed X-ray maps of SNR shells and partial spectra of high-energy cosmic rays measured by the surface particle detectors. The theoretical models of shock acceleration assuming shocks with various velocities propagating in the exited random magnetic fields can accelerate even particles up to 10^{17} eV (see review [24]). To reach these high energies, the particles should be trapped near the shock

wave to gain energy during numerous shock traversals. The proton and striped nuclei confinement near the shock is accounted for by scattering on the self-excited Alfvén waves [25].

We believe that the same mechanisms, operating at a much smaller scale, accelerate the solar cosmic rays [26] reaching the Earth and detected by the space-born and surface particle detectors. These direct relations of the acceleration mechanisms of solar and galactic cosmic rays and the growing understanding of the importance of solar–terrestrial connections contribute to the interest towards ground-based particle detection in Solar physics and Space Weather research [27–29].

It remains, however, very important to summarize and confirm the surface detectors findings to solve the CR source problem. In the presented paper, we clarify and check the EAS registration technique used for the MAKET-ANI data analysis. The most important quantity calculated from EAS measurements is the shower lateral distribution function (LDF). The shower size – N_e and shape (age) – s parameters are derived from the interpolated LDF and used for the primary particle type and energy estimation. We present the procedures used for calculating these parameters and discuss the accuracies and biasness of the estimates. We also present the size distribution of the measured showers, obtained with minimal assumptions about the strong interaction model.

The MAKET-ANI detector has been in operation for ~10 years and its experimental database contains more than 1.3 million showers with $N_e \geq 10^5$ and zenith angles $\leq 47^\circ$. The EAS database can be accessed from the home page of the Cosmic Ray Division of Yerevan Physics Institute (<http://crdlx5.yerphi.am>).

1. Experimental procedures for obtaining EAS parameters

The MAKET-ANI surface array [30], see Fig. 1, includes 92 particle density detectors consisting of 5 cm thick plastic scintillators. Sixty eight detectors have 1 m² area, the remaining 24 are 0.09 m². The central part of the detector consists of 73 scintillators and is arranged in a rectangle of 85 × 65 m². Fifteen and four 1 m² scintilla-

tors of the same type are placed at two remote locations at a distance of 95 m and 65 m from the center of the array. In order to estimate the zenith and azimuth angles, the 19 (9 of them participate in timing trigger) detectors out of 92 are equipped with timing readouts to measure the timing of the appearance of the EAS front with an accuracy of ~5 ns. The photomultiplier tubes (PM-49) of the detectors are placed in the light-tight iron boxes. Logarithmic analog to digital converters (ADC) and constant fraction discriminators (CFD) are assembled just above the photomultiplier tube (see Fig. 2). The dynamic range of the registered particle number is $\sim 5 \times 10^3$.

Three types of detector triggers are used:

1. The hardware trigger: at least 7 of 11 central density detectors must be hit by more than three particles.
2. The timing trigger: at least 4 from 9 preselected timing detectors, symmetrically arranged relative to the center of array, should be hit.
3. The software trigger adding several additional restrictions was used off-line.

If the first two conditions are fulfilled, the information from all 92 channels is stored. The trigger and data readout systems are implemented in the CAMAC standard. The simulations prove that the trigger system selects EAS with sizes $N_e \geq 10^5$ with cores located within the rectangle of 44 × 20 m² around the geometrical center of the detector with efficiency no less than 95% [31].

1.1. Accuracies of the EAS parameters determination

The EAS axis is assumed to follow the primary CR direction. In turn, the EAS direction is usually derived from the arrival time measurements applying fast-timing technique. In MAKET-ANI array 19 detectors are equipped with two PMs (see Fig. 2). One of them is used for particle density estimation, and the second – for the precise timing. The output signal from the timing channel (in the NIM standard) triggers the 200 MHz frequency generator. The signal of the timing trigger is used as a STOP signal. The quantification level for the timing infor-

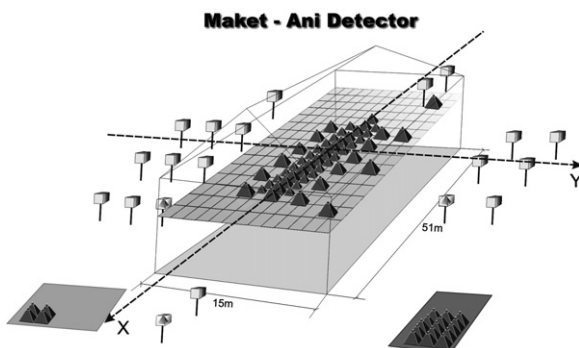


Fig. 1. The layout of the MAKET-ANI detector.

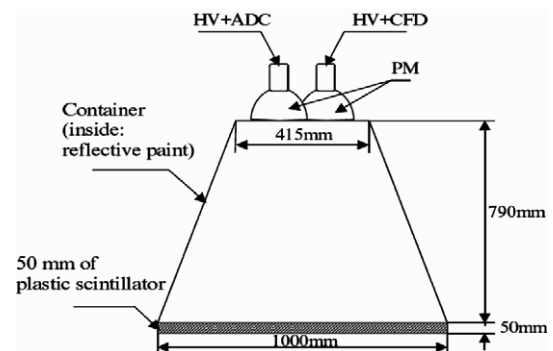


Fig. 2. The MAKET-ANI scintillator–PMT configuration for the 19 detectors with timing.

mation is 5 ns. A more detailed description of the fast-timing system can be found in [32].

The zenith θ and azimuth φ angles are defined by solving the following system of equations:

$$c \cdot \Delta t_i = (x_i \cdot \cos(\varphi) + y_i \cdot \sin(\varphi)) \cdot \sin(\theta) + z_i \cdot \cos(\theta),$$

$$i = 1, \dots, M \quad (1)$$

where c is the speed of light, Δt_i is the delay of the signal in the i th scintillator compared to a reference scintillator placed in the geometrical center of the array, x_i, y_i, z_i are the space coordinates and M is the number of timing detectors.

The estimates of angular accuracies were obtained by simulation of detector response (taking into account the triggers conditions, EAS size spectrum, etc.), assuming that the particles arrival time can be described by Gaussian distribution [33]. An independent method uses different possible combinations of timing detectors for calculating the angles of incidence. Then, from a variety of alternative estimates, the non-parametric estimate of variance was constructed according to [34]. Both methods give consistent results: angular accuracy no worse than $\sim 1.5^\circ$ for zenith angles and no worse than $\sim 5^\circ$ for the azimuth ones for the showers within $15^\circ < \theta < 45^\circ$ (see Fig. 3). The accuracy of the azimuth angle strongly depends on the zenith angle and becomes very poor at small zenith angles.

The analog signal from PM is converted to code using logarithmic ADC; the relative uncertainty introduced by the transition from analog signal to discrete code is $\sim 10\%$ [35].

The logarithmic ADC provides the linearity of the transformation (see Fig. 4), therefore we can write

$$K = \text{int}(d \cdot \ln A_{\text{PM}}) + K_0 \quad (2)$$

where K is the registered code (output of ADC), d is the scale factor of ADC (the so-called “decrement”), tuned

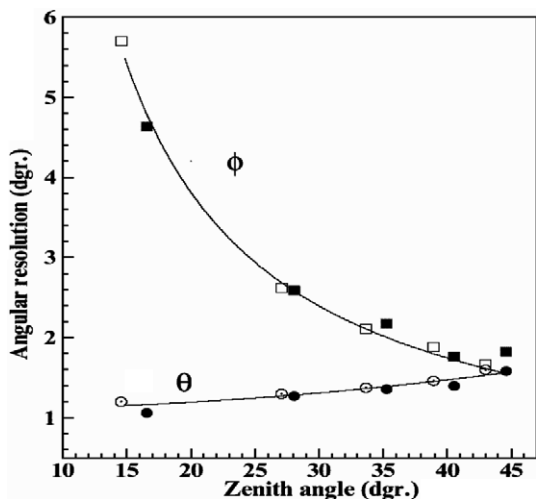


Fig. 3. The angular accuracies of the EAS axes determination. Rectangles – azimuth angles; circles – zenith angles. Open symbols – non-parametric method, closed symbols – simulation.

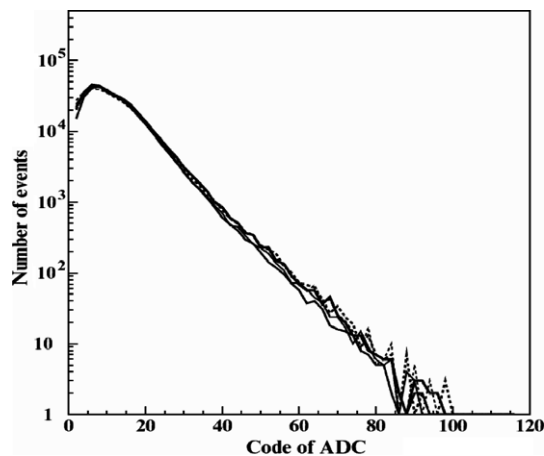


Fig. 4. The distribution of the registered ADC codes by four scintillators of the MAKET-ANI array.

with special electronics to be $d = 10 \pm 0.2$, and A_{PM} is the output signal of the PM. To give physical meaning to the registered code K , we define an arbitrary constant K_0 to be equal to the mean energy deposit of electrons in 5 cm thick scintillator. In this case, the quantity $e^{(K-K_0/d)}$ will be equal to the number of particles in the scintillator.

The simulations of EAS electrons traversal through the 5 cm thick scintillator with GEANT3 [80] code and calibration measurements of K_0 [36] provide very close value, ~ 10.8 MeV, of the mean energy release of the EAS electrons. Proceeding from this value, the conversion from the energy release to the detected code was done according to the methodology described in [37]. Using the detected code values, we determine the number of particles (density) at each 92 scintillator location. Then, using interpolation and integration procedures, we estimate the total number of electrons in the shower. We also have to correct the observed particle number registered by the scintillator to various effects such as the contamination of the electron–positron pairs borne by the traversing gamma ray in the scintillator, and nuclear interactions in the scintillator. The ratio between experimentally observed density $\rho_{\text{sc}}(r)$ and EAS electron density $\rho_{\text{ch}}(r)$ depends on the distance from the EAS axes and can be described as follows [38]:

$$R_{\text{sc/ch}}(r) = \rho_{\text{sc}}(r)/\rho_{\text{ch}}(r) = (r/r_m)^{-\alpha} \quad (3)$$

where r is the distance from the EAS core, r_m – Moliere radius, equal to 118 m on the MAKET-ANI array location and α is the parameter controlling the steepening of the function (3). We determine α from the measurements of particle densities by the 1.0, 1.5 and 5 cm thick scintillators located in the one and the same position [39]. For the EAS with the number of particles $N_e \geq 10^5$, we obtain value $\alpha \sim 0.18$ – 0.19 which agrees well with [40,41]. The accuracy of the measured particles density also depends on the fluctuations of the light collection in the scintillator, PM quantum efficiency, amplifier fluctuation, the accuracy of the scale factor estimation, etc. [37]. Influence of these effects on the density estimates was checked by comparing output

signals of two measuring channels (PM + ADC) attached to the same scintillator. Finally the total relative error of the particle number estimate comes to $\sim 11\%$ for five particles, $\sim 13\%$ for 500 particles and reaches $\sim 18\%$ at a maximal number of 5000 particles.

1.2. Detectors calibration and stability

It is necessary to periodically check the stability of array channels during multiyear observations. The drift of the characteristics of the components used for assembling the PM high voltage and ADC electronic devices leads to a bias in the particle density measurements, and, therefore, in EAS size and shape estimation. The MAKET-ANI detector was commissioned in the late 80s. The characteristics of the electronic components significantly degraded and need continuous check and replacement. The idea to use the fluxes of secondary cosmic rays produced by primaries in terrestrial atmosphere for the detector calibration is straightforward. It was much more complicated to choose the appropriate parameter of the secondary flux, stable enough to be used as a reference for at least 10 years. The problem is that our nearest star, the Sun, is modulating the low-energy CR flux. The modulation effects can be broadly categorized into three types. The first one relates to the acceleration of protons and ions in solar flares and by shock waves. If the energy of the accelerated particles is high enough, the solar cosmic rays produce additional muons and electrons enhancing the mean intensity measured by the surface particle detectors (the so-called ground level enhancement – GLE). These events are rather rare and their duration is usually no more than few tens of minutes at Aragats latitude. Other solar modulation effects relate to the transport of the huge magnetic cloud, ejected from Sun during violent explosions (coronal mass ejection – CME). Reaching the Earth, this cloud disturbs the terrestrial magnetic field and makes the intensity of the incident GCR decrease. The consequent decrease of the secondary cosmic rays is known as Forbush decrease (Fd) and can come close to 20% at Aragats latitudes [42]. At the recovery phase of Fd lasting for about a week, the intensity of secondary particles can show a peak lasting for several hours and coinciding with the sudden beginning of a severe geomagnetic storm (GMS). GMS originates due to the decrease of the terrestrial magnetic field interacting with CME magnetic field. This decrease leads to the entrance of additional low-energy protons and ions in the atmosphere and the generation of the additional secondary particles. Therefore, solar modulation effects, mostly long lasting Fd, can significantly change the intensity of the secondary cosmic ray flux, which cannot be used for detector calibration purposes. On the other hand, the spectra of the energy releases in scintillators measured by the ADC prove to be stable quantity, not influenced by even the strongest Fd.

Examining the change of the intensity of the secondary cosmic rays (see Fig. 5a), we detect that during the huge

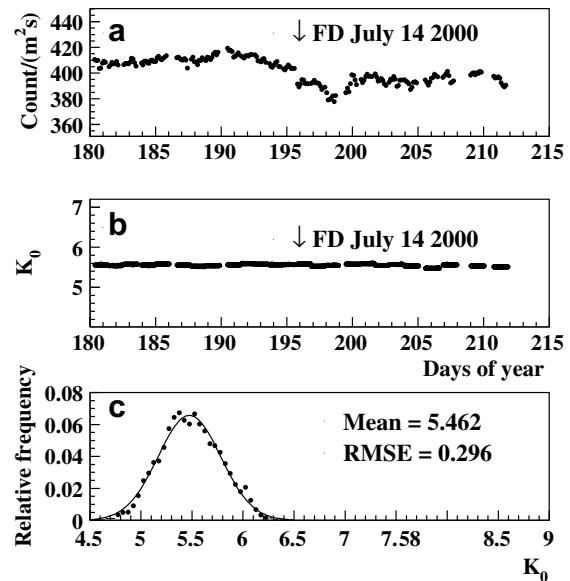


Fig. 5. Time series and histogram of the registered count rates of MAKET-ANI scintillators in July 2000. (a) Count rate of secondary particles per second. There is an abrupt decrease of intensity during Fd which started on July 14, 2000. (b) The time history of the mode of the energy release spectra K_0 , note that during the huge Fd on July 14 there are no changes. (c) Distribution of the obtained K_0 taken for all 92 scintillators of the array including $N_{\text{tot}} \approx 10^4$ measurements of K_0 .

Forbush decrease on July 14 the intensity decreased by $\sim 8\%$ and it took more than a week to recover its previous value. At the same time (see Fig. 5b) the mode of the spectra of secondary cosmic rays detected by 5 cm scintillator was very stable and did not change during Fd. Fig. 5c confirms the high stability of the chosen parameter. Therefore, the mode values of the spectra of energy release K_0^i (the so-called “single particle” spectrum) were monitored during the whole operation of MAKET-ANI for all 92 channels. After the regular examination of these parameters, if, for example, we find the value of K_0^i of the i th scintillator out of the acceptable limits of $5.5 \pm 3\sigma$ (see Fig. 5c), this particular scintillator signal did not enter EAS analysis procedures and its PM high voltage was tuned. In this way, the continuous check of the MAKET-ANI measuring channels provided high stability of array operation in 1997–2004.

1.3. Reconstruction of the EAS electron number

From the particle densities measured by the grid of array scintillators, it is possible to derive the total number of particles (the EAS size N_e), the center of gravity of the 2-dimensional particle density distribution (EAS core location), and, the so-called, s shower shape (age) parameter, correlated with the height of the first interaction of primary ion with the nuclei of terrestrial atmosphere. The functional form of the EAS lateral distribution was suggested by Nishimura, Kamata and Greizen (NKG) [43,44]:

$$\rho_{sc}(r) = N_e/r_m^2 \cdot C(s) \cdot R_{sc/ch} \cdot (r/r_m)^{s-2} \cdot (r/r_m + 1)^{s-4.5}, \quad (4)$$

where $\rho_{sc}(r)$ is the observed density at distance r from the EAS core position, N_e is the EAS size, $r_m = 118$ m (for the MAKET-ANI altitude) is the Moliere radius, s is the age of shower, $R_{sc/ch}$ – the correction factor (see Eq. (3)) and $C(s) = 0.366s^2(2.07 - s)^{1.25}$ is the normalization constant [45,46]. First, the iteration procedure is used to determine the EAS shape parameter s and core co-ordinates by least squares method (MINUIT [81]), then the shower size N_e is estimated by maximum likelihood method (see details in [47]).

Many authors [48,49] mention that the NKG function does not satisfactorily fit the electron density distribution at the large distances from the EAS core. It is not the case for MAKET-ANI, because the modest sizes of array allowed us to estimate the lateral distribution function at rather small distances not exceeding 120 m.

One of the checks of the EAS parameters reconstruction soundness is the uniformity test. Fig. 6 demonstrates that the reconstructed co-ordinates of EAS axes rather uniformly fill the surface occupied by the MAKET-ANI array. There are no pronounced gaps or peaks in the 2-dimensional distribution of the shower axes.

The event frequency (counts per minute) is also a very important parameter demonstrating the stability of the trigger condition during multiyear operation. Fig. 7 presents the 5-year time series of the frequencies of the detected EAS. The average frequencies of the selected EAS are very stable and equal to $0.234 \pm 0.013 \text{ min}^{-1}$ for $N_e \geq 1.6 \times 10^5$; $0.056 \pm 0.006 \text{ min}^{-1}$ for $N_e \geq 4 \times 10^5$ and $0.013 \pm 0.003 \text{ min}^{-1}$ for $N_e \geq 10^6$.

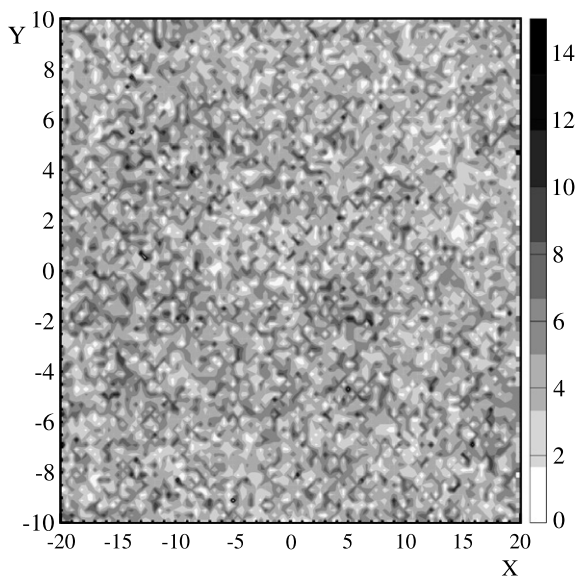


Fig. 6. A two-dimensional histogram of the EAS hits of MAKET-ANI array (1.5×10^5 events).

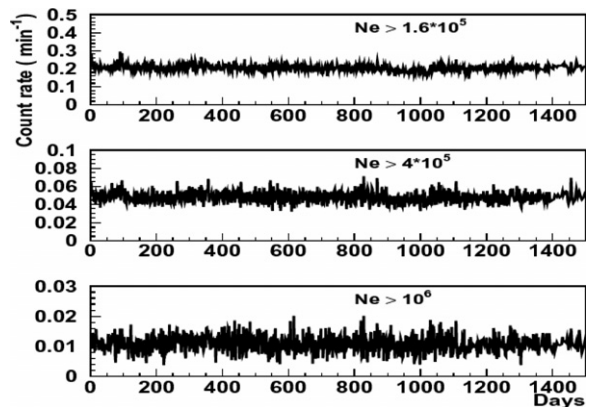


Fig. 7. The count rate of registered EAS versus exposition time since 1st June 1997 for different EAS sizes; core position is within the area of 880 m^2 .

1.4. The efficiency of EAS registration and array response to primary protons and iron nuclei

For a reliable reconstruction of the CR flux incident on the atmosphere, it is necessary to investigate the efficiency of the trigger. A simple event-generator (for details see [37,50]) simulates the EAS falling randomly on the rectangular area of 44×80 m. The shower sizes were simulated using the power law with constant power index $\gamma = -2.5$ for the EAS sizes starting from $N_e = 3.8 \times 10^4$. The zenith angle is assumed to follow $\text{Cos}^\beta(\theta)$ form, where $\beta = (X_0/\lambda)$, $X_0 = 700 \text{ g/cm}^2$, and $\lambda = 140 \text{ g/cm}^2$, the azimuth angle was simulated by the uniform distribution in $0-360^\circ$. Approximately 10^8 events were generated. For each event the number of shower particles at 92 detector locations was determined using NKG function. The shower age parameter was randomly chosen from the parameterized function obtained from the showers measured by MAKET-ANI. After obtaining NKG particle densities at all 92 array scintillator locations, they were distorted according to the experimental accuracies. Then the data analysis procedures adopted by the MAKET-ANI experiment were used (see points 1.1–1.3). The comparisons of the number “input” EAS and the “registered” EAS allow us to estimate the array efficiency to detect EAS with different sizes.

After obtaining the efficiencies for each shower size N_e , we determine the appropriate core selection areas (rectangles around the array geometrical center) to guarantee high ($\varepsilon \geq 0.95$) efficiency of the EAS registration. This allowed to define the so-called effective area S_{eff} , ensuring pre-selected registration efficiency for each shower size. Using appropriate S_{eff} areas for each N_e , the size spectra for different angles of incidence were obtained (see Section 4). The additional restriction requires the maximal allowable distortion of age parameter to be less than 0.03.

We also perform simulations to check the array response to the EAS initiated by primary proton, He, Si and iron nuclei. To avoid biases due to attenuation of EAS in terrestrial atmosphere and due to different responses of array to

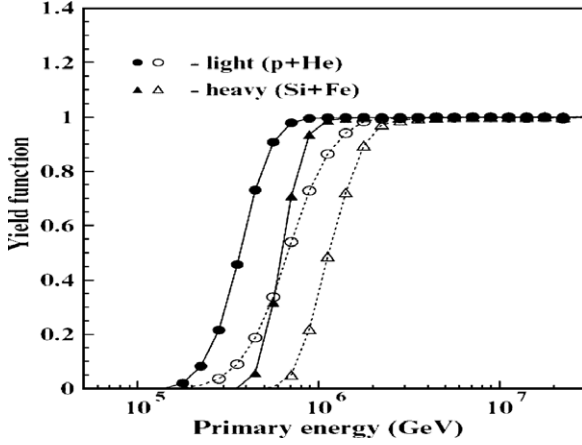


Fig. 8. The response of the MAKET-ANI detector on simulated “light” (p + He) and “heavy” (Si + Fe) induced showers, versus primary energy; shower selection criteria: $N_e \geq 10^5$, $\theta \leq 30^\circ$ (closed symbols), $N_e \geq 10^5$, $30^\circ \leq \theta \leq 45^\circ$ (open symbols).

“light” (p + He) and “heavy” (O + Si + Fe) primaries, the core selection area was limited to $20 \times 44 \text{ m}^2$ around the geometrical center of the array and showers with $N_e \geq 10^5$ coming from near vertical direction ($0^\circ \leq \theta \leq 30^\circ$) were selected. This made us lose some events. However (see Fig. 8, closed symbols), by making small corrections ($< 10\%$) to estimated intensities it is possible to obtain the unbiased “recovered” intensity of the “light” nuclei flux starting from $\sim 6 \times 10^{14} \text{ eV}$ and from $\sim 8 \times 10^{14} \text{ eV}$ for the “heavy” nuclei, respectively. For the inclined showers ($30^\circ \leq \theta \leq 45^\circ$), (see Fig. 8, open symbols), much larger corrections should be done. As a result, the reliability of the spectra reconstruction becomes debatable.

1.5. The accuracy of the EAS parameters estimation

The same event generator, as described in Section 1.4, was used for the estimation of the distortions of estimated shower parameters such as particles number N_e , shower age s and shower core position. The differences of the “input” EAS parameters ($N_e^{\text{sim}}, s^{\text{sim}}, R^{\text{sim}}(X, Y)$) and calculated ($N_e^{\text{rec}}, s^{\text{rec}}, R^{\text{rec}}(X, Y)$) ones are presented in Figs. 9 and 10. The reconstructed shower size errors (including systematic) are less than $\sim 13\%$ at $N_e = 10^5$ and quickly decrease with the rise of shower size. The systematic errors lead to the overestimation of the EAS size by $\sim 5\text{--}6\%$ at $N_e = 10^5$ and near 1% at $N_e \geq 10^6$.

The errors of reconstructed age parameter are less than $\sim 9\%$ at $N_e = 10^5$. The underestimation of s parameter is ~ 0.03 at $N_e \sim 10^5$. It turns to overestimation less than 0.01 at $N_e \sim 10^6$ and becomes vanishingly small at higher shower sizes. The accuracy of the reconstructed EAS core position within the collected area $S_{\text{eff}} = 880 \text{ m}^2$ is less than 1 m for all simulated age parameters and zenith angles of incidence. Shower parameters reconstruction errors (see Figs. 9 and 10) only slightly depend on the zenith angles of incidence.

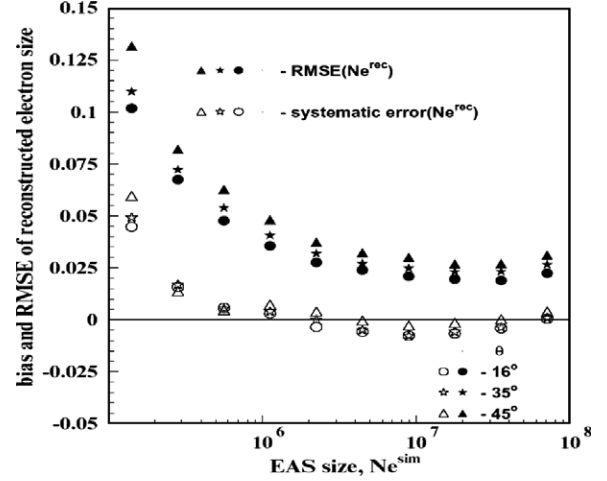


Fig. 9. The systematic errors and RMSE of shower size N_e^{rec} for different zenith angles of incidence.

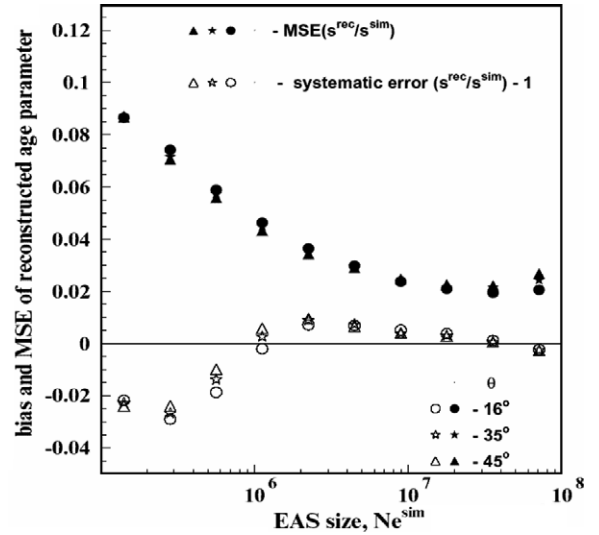


Fig. 10. The average difference (systematic error) and RMSE of ratio of reconstructed and simulated age parameter for the same zenith angles of incidence as in Fig. 9.

2. The EAS lateral distribution function (LDF)

From 1997 to 2004 $\sim 1.2 \times 10^7$ shower triggers were registered. The total exposition time was $\sim 1.42 \times 10^8 \text{ s}$. Only a small portion of the initial data was used for the investigation of the LDF and size and energy spectra in the presented analysis. We have already described how we selected the shower cores from the compact area around the geometrical center of the MAKET-ANI detector, ensuring large efficiency of EAS registration and high values of the “yield” function. This and additional restrictions on the EAS triggers

- $N_e \geq 10^5$,
- $0.3 < s < 1.7$,
- $\theta \leq 46.8^\circ$,

reduce the total number of events by an order of magnitude to a value of $\sim 1.3 \times 10^6$. Nonetheless, more than one million events with $N_e \geq 10^5$ are included in one of the largest data sets obtained by the EAS arrays operating at mountain altitudes.

The LDF functions were estimated in the five zenith angular intervals (bins), uniformly distributed according to $\text{Sec}(\theta)$ in $[0-46.8^\circ]$ and in nine logarithmically uniform intervals in shower size $\text{Lg} N_e [5-7.7]$ with step $\Delta \text{Lg}(N_e) = 0.3$. To avoid saturation effects, we did not use scintillators located at distances nearer than 10 m from EAS axes.

The analytical form of the LDF function is the major factor influencing the correct reconstruction of the shower size. The reconstructed size of EAS and the energy of primary particle are heavily dependent on the accepted assumption about LDF. Therefore, we first have to check the consistency of the chosen LDF shape by comparing the measured particle densities to those from the LDF best fit at detector location. The bias of density estimates is less than 5% for the core distances up to 80 m; it reaches $\sim 10\%$ at large distances ~ 120 m and large N_e ($\sim 10^7$) (see Fig. 11).

To compare the experimentally obtained LDF functions to the theoretical ones, we assume the following mass composition and energy spectra of the primary galactic cosmic rays (the so called “normal” mass composition [51]): (35% H , 25% He , 14% O , 15% Si , 10% Fe);

knee position $E_{\text{knee}} = Z \cdot E_0$, $E_0 = 3 \times 10^{15}$ eV, Z is the primary nuclei charge;

energy spectra index $\gamma_1 = -2.7$ before knee and, $\gamma_2 = -3.1$ after knee for all nuclei.

By simulating the EAS development in the atmosphere with the CORSIKA 562 (QGSJet01, NKG mode) code [52], we obtain the “pseudo-experimental” particle densities at scintillator locations. Using the experimental analysis procedures, we obtain the “theoretical” LDF functions.

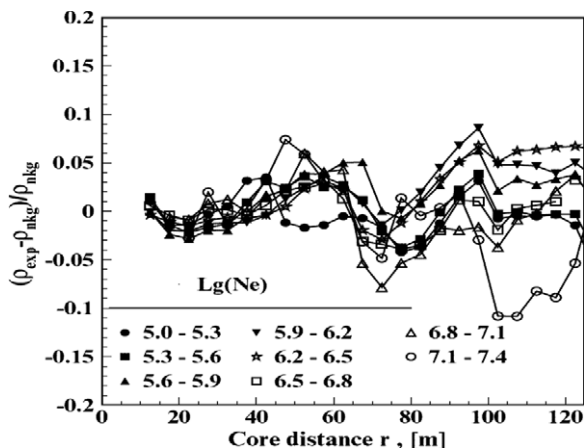


Fig. 11. The relative deviations of the experimentally observed showers particles LDF and expected by the NKG approximation for different EAS sizes.

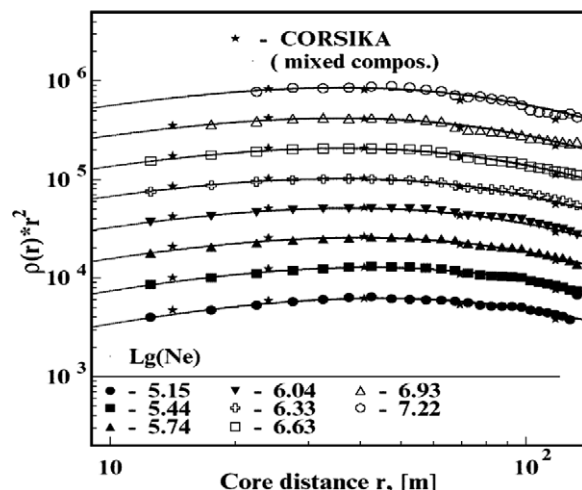


Fig. 12. The experimentally measured LDF in comparison to CORSIKA 562 (QGSJet01, NKG) simulations. The asterisks are “theoretical” values of the LDF function, the lines are LDF corresponding to the “averaged” EAS.

LDF functions are presented for different shower sizes in Fig. 12 for the near vertical EAS incidence $[0^\circ < \theta \leq 23.8^\circ]$. The experimental and “theoretical” values of LDF function agree quite well for all distances and for all shower sizes. The lines in Fig. 12 correspond to the LDF function obtained with the averaged EAS parameters measured in the experiment.

The high accuracies of the EAS parameters estimation (Figs. 9 and 10), the good agreement of the LDF obtained by CORSIKA simulations and the interpolation of the measured particle densities (Fig. 12) point to the soundness of using the experimental methodic to calculate

- array response;
- transition effects in the scintillators;
- EAS parameters.

3. Physical inference from the measured LDF

As we demonstrated in the previous section, the agreement of the measured LDF with CORSIKA, 562 simulations based on QGSJet01/NKG is quite good. The recently reported [12] disagreement of the measured LDF with that obtained by more sophisticated CORSIKA simulation modes (EGS mode with SIBYLL2.1 and with QGSJet01) can be explained by the drawbacks of strong interaction and electromagnetic cascading processes simulations. The better agreement of LDF measured by MAKET-ANI with that from NKG CORSIKA mode can be explained by the high latitude location of array (at the sea level the showers initiated by primaries of 10^{15} – 10^{16} eV are already attenuated and do not show “classical” NKG shape) and by much smaller EAS core collecting area. In this concern we want to mention once more that the used data analysis methods should be coherent

with (a) the information content of measurements and (b) the physical inference we want to derive from the experiment. We cannot treat simulations of EAS development in terrestrial atmosphere as a precise tool, therefore we have to restrict ourselves to robust physical inference which is efficient for deciding on the alternative physical hypothesis, but not too detailed and, as a result, not too heavily dependent on a particular simulation scheme and on the strong interaction model used.

The dependence of the measured age parameter on shower size in comparison to several models of primary flux composition is presented in Fig. 13. To outline the boundaries of the extreme cases we use pure proton and pure iron nuclei fluxes. More realistic assumptions about energy dependence of the primary composition are between these extreme assumptions:

1. Rigidity dependent “normal” composition with knee position at $E_{\text{knee}} = Z \cdot 3 \times 10^{15}$ eV [51].
2. The same as in point 1, but with fixed knee position at $E_{\text{knee}} = 3 \times 10^{15}$ eV for each group of nuclei.
3. “Heavy” composition (5% P, 5% He, 10% O, 10% Si, 70% Fe) [53], knee position at $E_{\text{knee}} = Z \cdot 3 \times 10^{15}$ eV.

For all three models the energy spectra index $\gamma_1 = -2.7$ before knee and $\gamma_2 = -3.1$ after knee for all nuclei.

The first model (“normal” composition) fits experimental data quite well (the value of the test equals $\chi^2 = 1.23$). At the same time we can exclude the options 2 ($\chi^2 = 8.8$) and 3 ($\chi^2 = 31.1$). The observed dependence of the age parameter on the EAS size (proxy of the energy of primary proton/nuclei) after knee can be understood as a result of the CR mass composition transition from light to heavy nuclear composition.

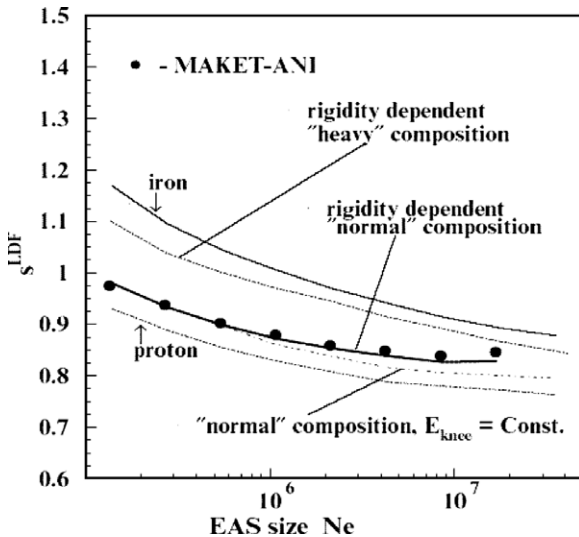


Fig. 13. The comparison of the $s(N_e)$ dependence measured by the MAKET-ANI array with different assumptions about primary flux composition.

4. Differential EAS size spectra

The size spectra presented in Table 1 are obtained with EAS collected from the area S_{eff} , providing a chosen level of the trigger efficiency ($>95\%$). We also keep the condition of the maximal allowable distortion of age parameter (<0.03) [31]. To check the detector response obtained with simple model (see Section 1.3), we use CORSIKA code to generate EAS for different nuclei, slopes of energy spectra and knee positions. The obtained results pointed to the model-independence of the used detector response function and to a correct account of the experimental distortions – the accuracy of the reconstructed spectral index was no worse than 0.01. In Table 1, the size spectra for five angular intervals uniform in $\text{Sec}(\theta)$ and 25 logarithmically uniform intervals in shower size are presented. The observed intensities were approximated by the equation suggested in [54]:

$$\frac{dJ(N_e, \theta)}{dN_e} = A(\theta) \cdot N_e^{-\gamma} \cdot \left[1 + \left(\frac{N_e}{N_e^{\text{knee}}} \right)^\delta \right]^{\Delta\gamma/\delta}, \quad (5)$$

where $A(\theta)$ is the angular dependence of the spectrum; $\Delta\gamma = \gamma_1 - \gamma$ is the change of power index; γ and γ_1 are the spectral indexes before and after knee; $N_e(\text{knee})$ is the knee position, and δ is the sharpness of the knee.

The parameters of approximation (5) of the size spectra, measured by MAKET-ANI, are listed in Table 2. From small values of goodness of fit χ^2/n df, we can conclude that Eq. (5) describes the size spectra quite well.

In Fig. 14, we present the size spectra measured by the MAKET-ANI detector along with the size spectra measured by the KASCADE experiment [55]. The numbers near the lines indicate the effective atmosphere depth, corresponding to different zenith angles of incidence. Knee positions for both MAKET-ANI and KASCADE data were calculated by Eq. (5). The change of the position of the knee with altitude, indicated by the solid line, demonstrates consistency of the major EAS parameters for both arrays located at sea level and at 3200 m above the sea level.

The remarkable coincidence of the size spectra measured by both detectors mentioned by Stanev [56] and large slant-depth available from joint data provide a well-established ground for attenuation length estimation. The longitudinal development of the electromagnetic fraction of EAS is characterized by the approximately exponential decrease in particle numbers for atmospheric depth far behind the shower maximum. Assuming a direct connection between the primary energy spectra and the electron number spectra, application of equal intensity cuts to integral electron number spectra in different angular bins selects showers with approximately equal primary energy. Measuring the attenuation of the electron number with increasing zenith angles yields the estimate of the attenuation length Λ_{N_e} . Proceeding from the knee positions indicated in Fig. 14 and the methodology described in [57], the attenuation length estimated by joint KASCADE–MAKET-ANI data

Table 1
The EAS intensities measured by the MAKET-ANI detector in 1997–2004

N_e	$S_{\text{eff}} \cdot T \times 10^{11}$ ($\text{m}^2 \text{s}$)	$dJ(\theta)/dN_e$ ($\text{m}^2 \text{s sr} \cdot N_e$) $^{-1}$ 0–23.8°	$dJ(\theta)/dN_e$ ($\text{m}^2 \text{s sr} \cdot N_e$) $^{-1}$ 23.8–32.4°	$dJ(\theta)/dN_e$ ($\text{m}^2 \text{s sr} \cdot N_e$) $^{-1}$ 32.4–38.5°	$dJ(\theta)/dN_e$ ($\text{m}^2 \text{s sr} \cdot N_e$) $^{-1}$ 38.5–43°	$dJ(\theta)/dN_e$ ($\text{m}^2 \text{s sr} \cdot N_e$) $^{-1}$ 43–46.8°
1.12×10^5	1.06	$(1.03 \pm 0.01) \times 10^{-10}$	$(6.56 \pm 0.01) \times 10^{-11}$	$(3.96 \pm 0.02) \times 10^{-11}$	$(2.50 \pm 0.02) \times 10^{-11}$	$(1.54 \pm 0.02) \times 10^{-11}$
1.41×10^5	–	$(5.70 \pm 0.01) \times 10^{-11}$	$(3.64 \pm 0.01) \times 10^{-11}$	$(2.24 \pm 0.01) \times 10^{-11}$	$(1.40 \pm 0.01) \times 10^{-11}$	$(8.81 \pm 0.10) \times 10^{-12}$
1.77×10^5	–	$(3.18 \pm 0.01) \times 10^{-11}$	$(2.02 \pm 0.01) \times 10^{-11}$	$(1.27 \pm 0.01) \times 10^{-11}$	$(7.96 \pm 0.08) \times 10^{-12}$	$(4.93 \pm 0.07) \times 10^{-12}$
2.23×10^5	–	$(1.77 \pm 0.01) \times 10^{-11}$	$(1.14 \pm 0.01) \times 10^{-11}$	$(7.27 \pm 0.06) \times 10^{-12}$	$(4.51 \pm 0.06) \times 10^{-12}$	$(2.85 \pm 0.05) \times 10^{-12}$
2.81×10^5	1.29	$(1.00 \pm 0.04) \times 10^{-11}$	$(6.45 \pm 0.04) \times 10^{-12}$	$(4.06 \pm 0.04) \times 10^{-12}$	$(2.55 \pm 0.03) \times 10^{-12}$	$(1.62 \pm 0.03) \times 10^{-12}$
3.53×10^5	–	$(5.61 \pm 0.03) \times 10^{-12}$	$(3.65 \pm 0.03) \times 10^{-12}$	$(2.33 \pm 0.03) \times 10^{-12}$	$(1.45 \pm 0.02) \times 10^{-12}$	$(9.19 \pm 0.20) \times 10^{-13}$
4.45×10^5	–	$(3.15 \pm 0.02) \times 10^{-12}$	$(2.05 \pm 0.02) \times 10^{-12}$	$(1.31 \pm 0.02) \times 10^{-12}$	$(8.46 \pm 0.15) \times 10^{-13}$	$(5.38 \pm 0.14) \times 10^{-13}$
5.60×10^5	–	$(1.77 \pm 0.01) \times 10^{-12}$	$(1.14 \pm 0.01) \times 10^{-12}$	$(7.51 \pm 0.11) \times 10^{-13}$	$(4.69 \pm 0.10) \times 10^{-13}$	$(2.85 \pm 0.09) \times 10^{-13}$
7.05×10^5	1.55	$(1.01 \pm 0.08) \times 10^{-12}$	$(6.60 \pm 0.07) \times 10^{-13}$	$(4.33 \pm 0.08) \times 10^{-13}$	$(2.68 \pm 0.06) \times 10^{-13}$	$(1.61 \pm 0.05) \times 10^{-13}$
8.87×10^5	1.83	$(5.62 \pm 0.05) \times 10^{-13}$	$(3.61 \pm 0.05) \times 10^{-13}$	$(2.40 \pm 0.04) \times 10^{-13}$	$(1.45 \pm 0.04) \times 10^{-13}$	$(8.48 \pm 0.32) \times 10^{-14}$
1.12×10^6	2.13	$(3.12 \pm 0.03) \times 10^{-13}$	$(2.03 \pm 0.03) \times 10^{-13}$	$(1.27 \pm 0.03) \times 10^{-13}$	$(7.63 \pm 0.21) \times 10^{-14}$	$(4.58 \pm 0.20) \times 10^{-14}$
1.41×10^6	2.46	$(1.73 \pm 0.02) \times 10^{-13}$	$(1.12 \pm 0.02) \times 10^{-13}$	$(6.80 \pm 0.16) \times 10^{-14}$	$(4.19 \pm 0.14) \times 10^{-14}$	$(2.38 \pm 0.12) \times 10^{-14}$
1.77×10^6	2.82	$(9.05 \pm 0.19) \times 10^{-14}$	$(5.78 \pm 0.11) \times 10^{-14}$	$(3.72 \pm 0.11) \times 10^{-14}$	$(2.14 \pm 0.09) \times 10^{-14}$	$(1.24 \pm 0.08) \times 10^{-14}$
2.23×10^6	–	$(5.06 \pm 0.08) \times 10^{-14}$	$(2.93 \pm 0.07) \times 10^{-14}$	$(1.95 \pm 0.07) \times 10^{-14}$	$(1.13 \pm 0.06) \times 10^{-14}$	$(6.41 \pm 0.47) \times 10^{-15}$
2.81×10^6	–	$(2.48 \pm 0.05) \times 10^{-14}$	$(1.59 \pm 0.05) \times 10^{-14}$	$(1.00 \pm 0.04) \times 10^{-14}$	$(5.95 \pm 0.38) \times 10^{-15}$	$(3.08 \pm 0.28) \times 10^{-15}$
3.54×10^6	–	$(1.30 \pm 0.03) \times 10^{-14}$	$(8.09 \pm 0.31) \times 10^{-15}$	$(5.06 \pm 0.28) \times 10^{-15}$	$(2.91 \pm 0.23) \times 10^{-15}$	$(1.76 \pm 0.21) \times 10^{-15}$
4.43×10^6	–	$(6.76 \pm 0.22) \times 10^{-15}$	$(4.08 \pm 0.19) \times 10^{-15}$	$(2.54 \pm 0.17) \times 10^{-15}$	$(1.50 \pm 0.15) \times 10^{-15}$	$(1.01 \pm 0.14) \times 10^{-15}$
5.59×10^6	–	$(3.47 \pm 0.13) \times 10^{-15}$	$(2.07 \pm 0.13) \times 10^{-15}$	$(1.11 \pm 0.10) \times 10^{-15}$	$(8.38 \pm 0.10) \times 10^{-16}$	$(4.39 \pm 0.78) \times 10^{-16}$
7.03×10^6	–	$(1.58 \pm 0.08) \times 10^{-15}$	$(1.07 \pm 0.08) \times 10^{-15}$	$(6.04 \pm 0.66) \times 10^{-16}$	$(3.17 \pm 0.61) \times 10^{-16}$	$(2.39 \pm 0.57) \times 10^{-16}$
8.87×10^7	–	$(8.36 \pm 0.53) \times 10^{-16}$	$(5.03 \pm 0.48) \times 10^{-16}$	$(4.28 \pm 0.51) \times 10^{-16}$	$(2.60 \pm 0.43) \times 10^{-16}$	$(1.26 \pm 0.38) \times 10^{-16}$
1.12×10^7	–	$(3.87 \pm 0.34) \times 10^{-16}$	$(2.97 \pm 0.35) \times 10^{-16}$	$(1.59 \pm 0.28) \times 10^{-16}$	$(1.41 \pm 0.30) \times 10^{-17}$	$(6.20 \pm 2.29) \times 10^{-17}$
1.39×10^7	–	$(2.31 \pm 0.22) \times 10^{-16}$	$(1.42 \pm 0.21) \times 10^{-16}$	$(1.03 \pm 0.10) \times 10^{-16}$	$(5.50 \pm 1.78) \times 10^{-17}$	$(4.89 \pm 1.61) \times 10^{-17}$
1.78×10^7	–	$(1.17 \pm 0.14) \times 10^{-16}$	$(9.30 \pm 1.39) \times 10^{-16}$	$(4.65 \pm 1.19) \times 10^{-17}$	$(1.58 \pm 0.79) \times 10^{-17}$	$(1.98 \pm 1.10) \times 10^{-17}$
2.20×10^7	–	$(6.04 \pm 0.92) \times 10^{-17}$	$(3.87 \pm 0.84) \times 10^{-17}$	$(3.26 \pm 0.92) \times 10^{-17}$	$(2.28 \pm 0.85) \times 10^{-18}$	$(2.10 \pm 0.99) \times 10^{-17}$
2.75×10^7	–	$(2.77 \pm 0.58) \times 10^{-17}$	$(2.77 \pm 0.59) \times 10^{-17}$	$(1.52 \pm 0.52) \times 10^{-17}$	$(8.20 \pm 4.80) \times 10^{-18}$	$(7.46 \pm 4.28) \times 10^{-18}$

The error bars are statistical. The systematic errors are presented in Figs. 9 and 10. The corrections according to calculated response function are made.

Table 2
Parameters of the size spectra measured by MAKET-ANI array

$\Delta\theta$ (degree)	γ	$\Delta\gamma$	N_e^{knee}	A	δ	χ^2 (n df)
0.0–23.8	2.53 ± 0.002	0.45 ± 0.02	$1.58 \times 10^6 \pm 8 \times 10^4$	641.79 ± 11	7.1 ± 1.7	1.1(19)
23.8–32.4	2.52 ± 0.002	0.43 ± 0.02	$1.33 \times 10^6 \pm 6 \times 10^4$	333.32 ± 8.5	11.6 ± 3.0	1.9(17)
32.4–38.5	2.47 ± 0.003	0.47 ± 0.03	$1.08 \times 10^6 \pm 8 \times 10^4$	114.37 ± 3.8	3.9 ± 0.8	1.2(19)
38.5–43.0	2.45 ± 0.003	0.45 ± 0.03	$0.86 \times 10^6 \pm 7 \times 10^4$	53.60 ± 2.6	4.36 ± 1.6	0.8(17)
43.0–46.8	2.44 ± 0.006	0.48 ± 0.04	$0.70 \times 10^6 \pm 6 \times 10^4$	29.18 ± 2.2	4.7 ± 1.4	0.9(16)

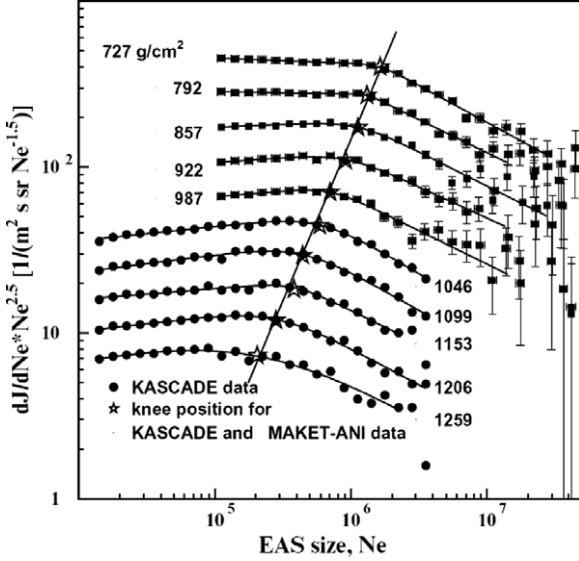


Fig. 14. The size spectra measured by MAKET-ANI and KASCADE experiments. The slant depth covered by experiments comprises 720–1250 g/cm². The solid line illustrates the EAS attenuation versus slant depth in the atmosphere.

covering the slant depth of 720–1250 g/cm² is equal to $A_{N_e} = 194 \pm 14$ g/cm², while by the MAKET-ANI data only it equals $A_{N_e} = 211 \pm 38$ g/cm², and by KASCADE– $A_{N_e} = 197 \pm 13$ g/cm² [58], accordingly. All estimates coincide within the error bars.

Taking into account the MAKET-ANI results when selecting light and heavy primary enriched EAS samples [8,34], we can pose the problem of estimation of attenuation length and other phenomenological parameters of strong interaction of primary nuclei with atmosphere for energies till 10^{16} eV.

5. The primary energy spectra

5.1. All particle energy spectrum

All particle energy spectrum is one of the major astrophysical parameters. Regardless of low sensitivity of its shape to models of the origin and acceleration of CR [1], the all particle spectrum is important as a commonly accepted benchmark for comparing different experiments or/and strong interaction models.

Size spectra and energy spectra are related to each other via sophisticated simulation, invoking nuclear-electromag-

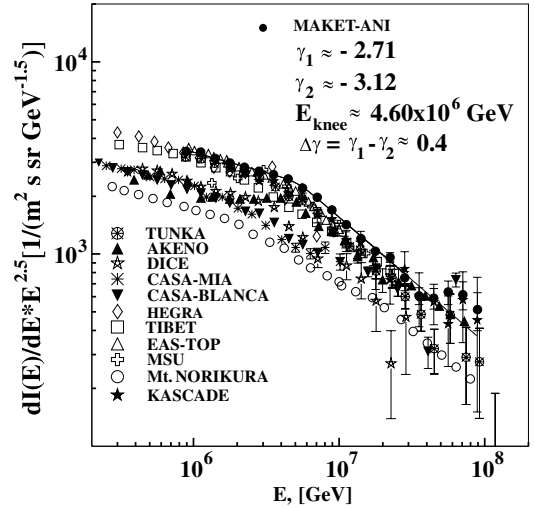


Fig. 15. The all particle spectrum from MAKET-ANI data compared to the world data. The line shows the fit to MAKET-ANI data according to Eq. (5) (integrated into 0–30° zenith angle interval). KASCADE [9], EAS-TOP [59], TIBET [60], HEGRA [61], AKENO [62], CASA-MIA [63], CASA-BLANCA [64], DICE [65], Mt. NORIKURA [66], MSU [67], and TUNKA [68].

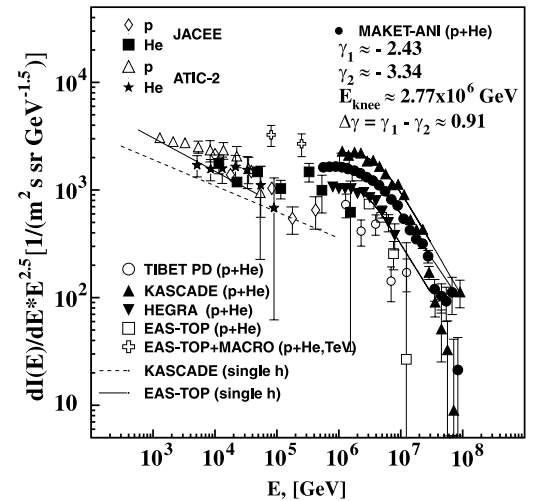


Fig. 16. Primary light component (p + He) measured by the MAKET-ANI detector in comparison to the results from KASCADE [9], EAS-TOP [72], HEGRA [10], EAS-TOP + MACRO [73], TIBET [74] and primary protons spectra approximations obtained by the single hadrons fluxes EAS-TOP [75] and KASCADE [76]. The direct balloon measurements by ATIC-2 [77] and JACEE [78] at 10^2 – 10^5 GeV are also presented.

netic cascade propagation in the atmosphere. As it was demonstrated in numerous KASCADE collaboration

papers (see [9]), the resulting energy spectrum depends on the particular high interaction model used in the simulation. Therefore, we should specify that the energy spectrum presented in Fig. 15 is obtained with CORIKA code (QGS-Jet01, NKG) mode. The very good agreement of spectra measured at the sea level and the mountain altitudes seen in Fig. 15 once more proves the maturity of the EAS experiments. It also proves reliability of the procedures used for the inverse problem solving.

The differential flux values of the primary particles energy spectra were obtained using the database of the sim-

ulated events obtained with CORSIKA 562 (QGSJet01, NKG) code [52] and applying the analysis and non-parametric inference (ANI) program package (described in [16,17]).

5.2. Partial energy spectra

The spectra of different mass groups were reported by MAKET-ANI and KASCADE data in 1999 [15]; and by EAS-TOP [69], HEGRA [10], TIBET AS γ [70], and KASCADE [71] at Hamburg ICRC in 2001. In [8], we present the spectra of light and heavy nuclei groups and come to the definite physical inference about a very sharp knee for the light component and the absence of knee at least up to 2×10^{16} eV for the heavy component. Now, after performing new checks of all possible experimental distortions (see above), we present the updated results on partial energy spectra with the enlarged data sample. For the energy estimation and EAS classification in “light” and “heavy” groups, we use the same statistical models from the “ANI” package as in 2004. The neural network models prove to be very powerful interpolation tool for data analysis in sophisticated multidimensional experiments (see references in [14]). Bayesian methods of classification also prove to be very powerful when model description cannot be supported by the definite analytical shape. By exposing the EAS parameters with known primary and energy to the classifying algorithm, we “train” the algorithm to recognize the experimental EAS without known primary and energy. As alternative classes (states of Nature) we include the “light” mass group showers initiated by the protons

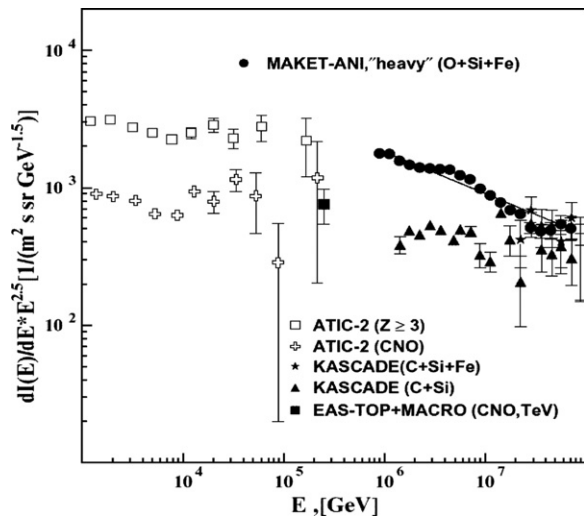


Fig. 17. The energy spectrum of the “heavy” nuclei group measured by the MAKET-ANI detector along with spectra from KASCADE [9], EAS-TOP + MACRO [73] and ATIC-2 [79]. The solid line is a power function approximation.

Table 3
The intensities of all CR, light and heavy nuclei groups

Energy (GeV)	$dJ/dE \pm \text{stat. errors} (\text{m}^{-2} \text{s}^{-1} \text{sr}^{-1} \text{GeV}^{-1})$ All particles	$dJ/dE \pm \text{stat. errors} (\text{m}^{-2} \text{s}^{-1} \text{sr}^{-1} \text{GeV}^{-1})$ Light	$dJ/dE \pm \text{stat. errors} (\text{m}^{-2} \text{s}^{-1} \text{sr}^{-1} \text{GeV}^{-1})$ Heavy
5.62×10^5	$(8.620 \pm 0.022) \times 10^{-12}$	$(6.920 \pm 0.019) \times 10^{-12}$	$(1.700 \pm 0.010) \times 10^{-12}$
7.07×10^5	$(6.716 \pm 0.017) \times 10^{-12}$	$(3.937 \pm 0.013) \times 10^{-12}$	$(2.779 \pm 0.011) \times 10^{-12}$
8.91×10^5	$(4.587 \pm 0.012) \times 10^{-12}$	$(2.224 \pm 0.009) \times 10^{-12}$	$(2.362 \pm 0.009) \times 10^{-12}$
1.12×10^6	$(2.582 \pm 0.008) \times 10^{-12}$	$(1.236 \pm 0.005) \times 10^{-12}$	$(1.346 \pm 0.006) \times 10^{-12}$
1.41×10^6	$(1.342 \pm 0.005) \times 10^{-12}$	$(6.707 \pm 0.038) \times 10^{-13}$	$(6.722 \pm 0.038) \times 10^{-13}$
1.77×10^6	$(7.157 \pm 0.035) \times 10^{-13}$	$(3.638 \pm 0.025) \times 10^{-13}$	$(3.520 \pm 0.025) \times 10^{-13}$
2.23×10^6	$(3.821 \pm 0.023) \times 10^{-13}$	$(1.936 \pm 0.016) \times 10^{-13}$	$(1.886 \pm 0.016) \times 10^{-13}$
2.81×10^6	$(2.050 \pm 0.015) \times 10^{-13}$	$(1.004 \pm 0.010) \times 10^{-13}$	$(1.046 \pm 0.011) \times 10^{-13}$
3.54×10^6	$(1.104 \pm 0.010) \times 10^{-13}$	$(5.238 \pm 0.067) \times 10^{-14}$	$(5.810 \pm 0.070) \times 10^{-14}$
4.46×10^6	$(5.908 \pm 0.063) \times 10^{-14}$	$(2.676 \pm 0.043) \times 10^{-14}$	$(3.232 \pm 0.047) \times 10^{-14}$
5.62×10^6	$(2.986 \pm 0.040) \times 10^{-14}$	$(1.323 \pm 0.027) \times 10^{-14}$	$(1.664 \pm 0.030) \times 10^{-14}$
7.07×10^6	$(1.501 \pm 0.025) \times 10^{-14}$	$(6.253 \pm 0.163) \times 10^{-15}$	$(8.761 \pm 0.194) \times 10^{-15}$
8.91×10^6	$(7.305 \pm 0.158) \times 10^{-15}$	$(3.073 \pm 0.102) \times 10^{-15}$	$(4.233 \pm 0.121) \times 10^{-15}$
1.12×10^7	$(3.459 \pm 0.097) \times 10^{-15}$	$(1.323 \pm 0.059) \times 10^{-15}$	$(2.136 \pm 0.076) \times 10^{-15}$
1.41×10^7	$(1.640 \pm 0.059) \times 10^{-15}$	$(5.770 \pm 0.351) \times 10^{-16}$	$(1.064 \pm 0.048) \times 10^{-15}$
1.77×10^7	$(7.888 \pm 0.037) \times 10^{-16}$	$(2.623 \pm 0.211) \times 10^{-16}$	$(5.265 \pm 0.299) \times 10^{-16}$
2.23×10^7	$(4.073 \pm 0.235) \times 10^{-16}$	$(1.326 \pm 0.134) \times 10^{-16}$	$(2.748 \pm 0.193) \times 10^{-16}$
2.81×10^7	$(1.827 \pm 0.140) \times 10^{-16}$	$(6.020 \pm 0.804) \times 10^{-17}$	$(1.226 \pm 0.115) \times 10^{-16}$
3.54×10^7	$(8.368 \pm 0.845) \times 10^{-17}$	$(1.622 \pm 0.372) \times 10^{-17}$	$(6.746 \pm 0.759) \times 10^{-17}$
4.46×10^7	$(4.409 \pm 0.547) \times 10^{-17}$	$(7.461 \pm 2.249) \times 10^{-18}$	$(3.663 \pm 0.499) \times 10^{-17}$
5.62×10^7	$(2.747 \pm 0.385) \times 10^{-17}$	$(4.310 \pm 1.524) \times 10^{-18}$	$(2.317 \pm 0.353) \times 10^{-17}$
7.79×10^7	$(1.540 \pm 0.257) \times 10^{-17}$	$(2.995 \pm 1.132) \times 10^{-18}$	$(1.241 \pm 0.230) \times 10^{-17}$
8.91×10^7	$(6.799 \pm 1.520) \times 10^{-18}$	$(3.399 \pm 3.399) \times 10^{-19}$	$(6.459 \pm 1.482) \times 10^{-18}$

and Helium nuclei and the “heavy” mass group showers initiated by Silicon and Iron nuclei. Before the Neural classification of the MAKET-ANI data, we investigate the expected purity and efficiency of the data analysis procedures. The purity and the efficiencies are obtained by classifying $\sim 35,000$ light (p, He) and $\sim 17,000$ heavy (O, Si, Fe) control events, which are not used for the training of the neural network. Neural classifier selects the “light” component with the efficiency $\sim 75\%$, purity $\sim 85\%$ and the “heavy” component with efficiency $\sim 75\%$, purity $\sim 57\%$. To understand how the “light” and “heavy” classes are “populated” by different nuclei, we assume a “normal” mass composition. The results of the classification of this mixture are as following:

Light group: 40% protons, 30% He, 14% O, 11% Si and 5% Fe;

Heavy group: 16% protons, 17% He, 20% O, 26% Si, and 21% Fe.

The energy of the two distinct classes of showers was estimated for each group separately, once more using CORSIKA simulation and neural estimation procedures.

From Fig. 16 it is apparent that the proton acceleration mechanism starts to fade after 10^{15} eV. The MAKET-ANI spectrum demonstrated this effect rather clearly, because of its pretty low threshold at $\sim 6 \times 10^{14}$ eV. The lower energy spectra of light nuclei obtained by the balloon experiments JACEE [78] and ATIC-2 [77] are consistent with the spectra obtained in EAS experiments, proving stability of the power index before the “knee” feature.

Fig. 17 presents the energy spectra of the “heavy” nuclei group obtained by MAKET-ANI, KASCADE [9] and EAS-TOP + MACRO [73] detectors along with direct measurement of ATIC-2 [79]. In contrast to “light” nuclei group energy spectra (Fig. 16), at least up to 10^{16} eV we did not see any feature demonstrating weakening of heavy nuclei acceleration. All particle spectrum and partial energy spectra measured by MAKET ANI experiment are posted in Table 3.

6. Conclusions

From 1997 up to the end of 2004, the MAKET-ANI experiment has taken data with exposition time of $\sim 1.46 \times 10^8$ s. The total number of the registered shower events was $\sim 1.2 \times 10^7$. A smaller sample of the data ($\sim 1.3 \times 10^6$) with $N_e \geq 10^5$ and $\theta \leq 46.8^\circ$ was used for the in-depth analysis of the LDF and size spectra. By 7.2×10^5 near the vertical EAS ($\theta \leq 30^\circ$), the energy spectra of light and heavy nuclei groups were obtained.

The experimental procedures of physical inference from the MAKET-ANI surface array have been considerably improved, due to the redundant data which allow for important consistency checks. Regular calibrations and cross calibrations, tests of efficiency and uniformity in detector response proved to be essential for retaining data

stability and reliability. The published papers on the size and energy spectra usually do not report the methodical errors, which leads to rather large discrepancies in the results. To overcome this drawback and to present methodical procedures with details allowing to judge about the achievable accuracies, we present all relevant procedures used when treating the MAKET-ANI data.

The extension of the experimental statistics, as compared to the previously reported analysis, allows us to present the size spectra and energy spectra of light and heavy components of primary cosmic ray flux in tables and graphs available for the physical inference about the CR origin and acceleration mechanisms.

- The obtained dependence of the shower age on shower size pointed to the weighting of the primary flux mass composition after the knee of the “all particle” spectrum.
- The size spectra show evidence of a “knee” at shower size $\sim 10^6$ particles. As the zenith angle enlarges, the knee position moves to smaller sizes, according to the EAS attenuation length $A_{N_e} = 211 \pm 38$ g/cm².
- The difference of the power law spectra before and after the knee is constant with high precision $\Delta\gamma = 0.45 \pm 0.02$.

The following experimental results from partial energy spectra of light and heavy mass groups measured in the MAKET-ANI experiment provide evidence in favor of the rigidity-dependent acceleration at the outer boundaries of SNR:

- The estimated energy spectrum of the light mass group of nuclei shows a very sharp knee: $\Delta\gamma \approx 0.9$, compared to $\Delta\gamma \approx 0.4$ for the all-particle energy spectra.
- The energy spectrum of the heavy mass group of cosmic rays shows no knee in the energy interval of 10^{15} – 10^{16} eV.

The mentioned results are consistent with the non-linear kinetic theory of CR acceleration in SNR shells [20].

Acknowledgements

We thank the staff of Mt. Aragats Cosmic Ray Observatory who contributed to the MAKET-ANI experiment implementation. We also thank ANI collaboration members for their fruitful cooperation over many years. This work was supported by Armenian Government grants and the ISTC A – 1058 grant.

References

- [1] J. Hoerandel, *Astropart. Phys.* 21 (2004) 241.
- [2] A. Haungs, H. Rebel, M. Roth, *Rep. Prog. Phys.* 66 (2003) 1145.
- [3] A. Chilingarian, *Comput. Phys. Commun.* 54 (1989) 31.
- [4] A. Chilingarian, M. Zazyan, *IL Nuovo Cimento* 14C (6) (1991) 555.

- [5] A. Chilingarian, *Neurocomputing* 6 (1994) 497.
- [6] A. Chilingarian, *Pattern Recog. Lett.* 16 (1995) 333–338.
- [7] C.M. Bishop, *Neural Networks for Pattern Recognition*, Oxford Univ. Press, New York, 1995.
- [8] A. Chilingarian, G. Hovsepyan, et al., *ApJ* 603 (2004) L29.
- [9] T. Antoni et al., (KASCADE), *Astropart. Phys.* 24 (2005) 1.
- [10] D. Horns et al., (HEGRA), in: *Proc. 27th ICRC, Hamburg*, vol. 1, 2001, p. 101.
- [11] M. Aglietta, B. Alessandro, et al., (EAS-TOP + MACRO), *Astropart. Phys.* 20 (2004) 641.
- [12] W.D. Apel et al., (KASCADE), *Astropart. Phys.* 24 (2006) 467.
- [13] A.M. Hillas, *Cosmic Rays: Recent Progress and some Current Questions*, arXiv:astro-ph/0607109, vol. 1, 2006.
- [14] A. Chilingarian, A. Vardanyan, et al., *NIMA* 502 (2003) 787.
- [15] A. Vardanyan, A. Chilingarian, M. Roth, (KASCADE), in: *Proc. of the Workshop ANI 99, Nor-Amberd*, Preprint FZK 6472, 2000, p. 23.
- [16] T. Antoni et al., *Astropart. Phys.* 16 (2002) 245.
- [17] T. Antoni et al., (KASCADE), *Astropart. Phys.* 19 (2003) 715.
- [18] M.A. Maljkov, L.O.C. Drury, *Rep. Prog. Phys.* 64 (2001) 429.
- [19] K.S. Long, S.P. Reynolds, J.C. Raymond, *ApJ* 586 (2003) 1162.
- [20] E.G. Berezhko, L.T. Ksenofontov, H.J. Volk, *A&A* 412 (2003) 11.
- [21] H.J. Volk, E.G. Berezhko, L.T. Ksenofontov, in: *Proc. 29th ICRC, Pune*, vol. 3, 2005, p. 233.
- [22] F.A. Aharonian et al., *Science* 307 (2005) 1938.
- [23] H. Katagiri et al., *ApJ* 619 (2005) L163.
- [24] V.S. Ptuskin, in: *Proc. 29th ICRC, Pune*, vol. 10, 2005, p. 317.
- [25] A. Marcowith, G. Pelletier, M. Lemoine, *Proc. 29th ICRC, Pune*, vol. 3, 2005, p. 221.
- [26] M.J. Aschwanden, in: N. Gopalswamy (Ed.), *AGU Monograph of AGU Chapman Conference, Turku, Finland, 2–6 August 2004*.
- [27] A. Chilingarian et al., in: *Proc. of the European High Energy Physics School, ESHEP, Tcakhkadzor, Armenia*, 2003.
- [28] S.N. Karpov, Z.M. Karpova, Yu.V. Balabin, E.V. Vashenyuk, in: *Official CD of 29th ICRC, Pune*, 2005.
- [29] J. Poirier, C.J. D’Andrea, *Geophys. Res., Space Phys.* 107 (A11) (2002) 1376.
- [30] E.V. Bazarov et al., *VANI T, Ser. Nucl. Phys. Reser.* 5 (31) (1986) 3 (in Russian).
- [31] G. Hovsepyan, A. Chilingarian et al., in: *Proc. 29th ICRC, Pune*, vol. 6, 2005, p. 93.
- [32] A.D. Yerlikin et al., *VANI T Ser. Nucl. Phys. Reser.* 4 (4) (1998) 3 (in Russian).
- [33] J. Linsley, in: *Proc. 19th ICRC*, vol. 7, 1985, p. 359.
- [34] A. Chilingarian et al., in: *Proc. 27th ICRC, Hamburg*, vol. 2, 2001, p. 590.
- [35] A. Daryan et al., *Preprint YerPhI*, vol. 1485(2)-97, 1997, p. 13 (in Russian).
- [36] E.A. Mnatsakanyan et al., *Preprint YerPhI*, N 1610(8)-06, 2006 (in Russian).
- [37] G. Hovsepyan, in: *Proc. of the Workshop ANI 98, FZKA 6215, Forschungszentrum Karlsruhe*, 1999, p. 41.
- [38] V.S. Murzin, *Introduction to Cosmic Ray Physics*, Moscow, 1979, 275p. (in Russian).
- [39] S. Blokhin et al., *Proc. of the Workshop ANI 99, FZKA 6472*, 2000, p. 111.
- [40] T.P. Amineva et al., *Izv. AN, Ser. Phys.* 33 (1968) 1508 (in Russian).
- [41] J.H. Weber et al., (KASCADE), in: *Proc. 25th ICRC (Durban)*, vol. 6, 1997.
- [42] A. Chilingarian, K. Avagyan, et al., *Adv. Space Res.* 31 (2003) 861.
- [43] K. Greisen, *Prog. Cosmic Ray Phys.*, vol. 3, North Holland Publ., 1956.
- [44] K. Kamata, J. Nishimura, *Progr. Theoret. Phys.* 6 (Supp.) (1958) 93.
- [45] S. Hayakawa, *Cosmic Ray Physics*, *Cosmic Ray Physics, Interscience Monographs and Texts in Physics and Astronomy*, vol. 22, Wiley-Interscience, 1969.
- [46] V.S. Aseykin et al., *Lebedev Inst. Proc.* 109 (1979) 3 (in Russian).
- [47] G. Gharagozyan, in: *Proc. of the Workshop ANI 98, FZKA*, preprint 6215, 1999, p. 51.
- [48] S. Yoshida et al., *Phys. G: Nucl. Part. Phys.* 20 (1994) 651.
- [49] A.V. Glushkov et al., in: *Proc. 25th ICRC, Durban*, vol. 6, 1997, p. 233.
- [50] G. Hovsepyan, ANI collab. report No. 5, 2001, <http://crdlx5.yerphi.am/ani-collab.html>.
- [51] G.B. Kristiansen et al., *Astropart. Phys.* 2 (1994) 127.
- [52] D. Heck et al., *FZKA report 6019, Forschungszentrum, Karlsruhe*, 1998.; N. Kalmikov, S. Ostapchenko, A. Pavlov, *Nucl. Phys. B (Proc. Suppl.)* 52B (1997) 17.
- [53] E. Juliusson, in: *13th ECRC, Geneva*, vol. OG-6, 1993, p. 11.
- [54] S. Ter-Antonyan, L. Haroyan, *hep-ex/0003006*, 2000.
- [55] R. Glasstetter et al., (KASCADE), in: *Proc. 25th ICRC, Durban*, vol. 2, 1997.
- [56] T. Stanev, in: *American Institute of Physics (AIP), Conference Proceedings*, vol. 516, 2001, p. 247.
- [57] S. Sokhoyan et al., in: *Proc. 27th ICRC, Hamburg*, vol. 1, 2001, p. 165.
- [58] G. Maier et al., (KASCADE), in: *Proc. 27th ICRC, Hamburg*, vol. 1, 2001, p. 161.
- [59] M. Aglietta et al., (EAS-TOP), *Astropart. Phys.* 10 (1999) 1.
- [60] M. Amenomori et al., (TIBET), *Astrophys. J.* 461 (1996) 408.
- [61] F. Arqueros et al., (HEGRA), *Astron. Astrophys.* 359 (2000) 682.
- [62] M. Nagano et al., (AKENO), *J. Phys. G: Nucl. Part. Phys.* 10 (1984) 1295.
- [63] M.A.K. Clasmacher et al., (CASA-MIA), *Astropart. Phys.* 10 (1999) 291.
- [64] J.W. Fowler et al., (CASA-BLANKA), *Astropart. Phys.* 15 (2001) 49.
- [65] S.P. Swordy, D.B. Kieda, (DICE), *Astropart. Phys.* 13 (2000) 137.
- [66] N. Ito et al., (Mt. NORIKURA), in: *25th ICRS, Durban*, vol. 4, 1997, p. 117.
- [67] Y.A. Fomin et al., (MSU), in: *22nd ICRC, Dublin*, vol. 2, 1991, p. 85.
- [68] N.M. Budnev et al., (TUNKA), in: *Proc. 29th ICRC, Pune*, vol. 6, 2005, p. 257.
- [69] B. Alessandro et al., (EAS-TOP + MACRO), in: *Proc. 27th ICRC, Hamburg*, vol. HE1.02, 2001, p. 124.
- [70] M. Amenomori et al., (TIBET), in: *Proc. 27th ICRC, Hamburg*, vol. HE1.02, 2001, p. 148.
- [71] H. Ulrich et al., (KASCADE), in: *Proc. 27th ICRC, Hamburg*, vol. HE1.02, 2001, p. 97.
- [72] M. Aglietta et al., (EAS-TOP), *Astropart. Phys.* 21 (2004) 583.
- [73] M. Aglietta et al., (EAS-TOP + MACRO), *Astropart. Phys.* 21 (2004) 223.
- [74] M. Amenomori et al., (TIBET), *Phys. Lett. B* 632 (2006) 58.
- [75] M. Aglietta et al., (EAS-TOP), *Astropart. Phys.* 19 (2003) 329.
- [76] T. Antoni et al., (KASCADE), *ApJ* 24 (2004) 1.
- [77] J.P. Wefel et al., (ATIC-2), in: *Proc. 29th ICRC, Pune*, vol. 3, 2005, p. 105.
- [78] K. Asakimori et al., (JACEE), *ApJ* 502 (1998) 278–283.
- [79] A.D. Panov et al., (ATIC-2), arXiv:astro-ph/0612377, vol. 1, 2006.
- [80] GEANT: CERN Program library Long Writeup W5013, CERN, 1993.
- [81] MINUIT: CERN Program Library Long Writeup, D506, CERN, 1993.